Materials and Methods

Preparation of Isotope-Labeled Amino Acids

$^{13}C^{18}O$ labeled glycine and L-valine were prepared starting from Gly-1-^{13}C and L-Val-1-^{13}C (Cambridge Isotope Laboratories) and ^{18}O water (Isotec) as described previously (*36*). Following ^{18}O exchange, the amino group was protected by *tert*-butyloxycarbonyl (Boc) for use in solid phase peptide synthesis (SPPS). Boc protection of Gly was carried out as previously described (*37*). Boc protection of the $^{13}C^{18}O$ labeled valine was carried out as follows. To a magnetically stirred mixture of 2 mmol of labeled Val in anhydrous MeOH (2.7 mL) containing 20% Et_3N, 2.4 mmol of Boc-anhydride was added followed by heating to 48°C. The reaction was allowed to proceed until all the amino acid dissolves. The reaction was stirred for an additional 30 min, following which the solvent was removed under reduced pressure. The crude reaction mixture was stirred for 10 min at 4 C with 2.5 mL of cold dilute hydrochloric acid (pH 2.15), and then extracted immediately with ethyl acetate (5 x 10 mL). The organic layer was dried over Na_2SO_4, the solvent was removed under reduced pressure and $^{13}C^{18}O$ –Boc-L-Val was purified by silica gel column chromatography (5% MeOH in chloroform).

Strategy for the synthesis of the isotope-labeled KcsA channel.

We used the modular semisynthesis approach for the assembly of the $^{13}C^{18}O$ labeled KcsA channel (*22*). In this approach, the channel is assembled from a synthetic pore peptide (residues 70-81 of the KcsA channel) and two recombinant peptides: a thioester peptide corresponding to residues 1-69 (N-peptide) and an N-terminal Cys peptide corresponding to residues 82-160 (C-peptide) by two sequential native chemical ligation reactions (NCL) followed by in vitro folding as shown in Fig. S1.

Expression and Purification of the N-peptide and the C-peptide

The protocols used for the recombinant expression and purification of the N- peptide have been previously described and were used without modification (*38*). For the C-peptide, we used the SUMO fusion/proteolysis approach (*22*). We constructed a fusion protein construct consisting of the yeast SUMO protein (residues 1-98) followed by the C-peptide (residues 82-160 of the KcsA channel with a Y82C substitution). The sumo fusion protein also consisted of a His_6 tag at the N-terminus and the following sequence LVPRGSSAWSHPQKEKA at the C-terminus, which encodes a thrombin site followed by a Strep tag. The fusion protein was expressed in *Escherichia coli* Rosetta2 (DE3) cells using the high-density expression protocol (*39*). Purification of the sumo fusion protein using metal affinity chromatography and cleavage using sumo protease was carried out as previously described (*22*). The C-peptide obtained after proteolysis was de-protected using 0.5 M methoxylamine (*40*) and purified by RP-HPLC on a preparative C4 column using a 50 – 100% gradient of buffer B (9:1 acetonitrile:H2O + 0.1%

TFA) and confirmed by Electrospray Ionization Mass Spectrometry (ES-MS) (observed mass = 10609.2 ± 1.9, expected = 10610.1).

Synthesis of the triple $^{13}C^{18}O$ labeled pore peptide.

The KcsA pore peptide (residues 70-81) Thz-ETATTVGYGDL-COSR which contains the selectivity filter sequence was assembled by manual solid phase peptide synthesis and purified as previously described (*22*). Thz refers to the 1, 3-thiazolidine-4-carboxo group. The $^{13}C^{18}O$ isotopically labeled amino acids were used at the underlined positions. The peptides were purified by RP-HPLC on a preparative C18 column using a 15 – 40% gradient of buffer B and confirmed by ES-MS [observed mass = 1337.7 ± 0.1 (M + H), expected = 1338.3 (M + H)].

Semisynthesis of the isotope-labeled KcsA channel.

The assembly of the KcsA polypeptide was carried out by two sequential NCL reactions. The first NCL reaction between the isotope labeled pore peptide and the C-peptide to form the intermediate peptide was carried out in 0.1 M sodium phosphate buffer at pH 7.5, 5 mM TCEP and1% (w/v) Fos-12 choline. The reaction was initiated by the addition of 2% (v/v) thiophenol and carried out at 37°C with gentle shaking. The reaction was monitored by SDS – PAGE and was generally complete in 2 - 4 hours. Following the first ligation reaction, the Thz group at N-terminus of the intermediate peptide was converted to Cys by treatment with 0.5 M methoxylamine (*40*). The deprotected intermediate peptide was purified by RP-HPLC on a C4 preparative column using a 50 – 100 % gradient of buffer B and confirmed by ES-MS (observed mass = 11829.5 ± 1.6, expected = 11830.4).

The second ligation reaction between the intermediate peptide and the N-peptide thioester to form the KcsA polypeptide was carried out in 0.1 M sodium phosphate buffer at pH 7.5, 5 mM TCEP, 1% (w/v) Fos-12 choline, 2% (v/v) thiophenol at 37°C with gentle shaking and monitored by SDS-PAGE. The ligation reaction was allowed to proceed for 12-24 hours and then terminated by the addition of DTT to 0.1 M. The semisynthetic KcsA polypeptide was folded to the tetrameric state using the previously described in vitro folding protocol for the KcsA channel (*38*).

Following *in vitro* folding, the lipid vesicles were solubilized using decyl maltoside (DM, 2% w/v), and the KcsA channel was purified by immobilized metal affinity chromatography. The His$_6$ tag present at the N-terminus was removed by proteolysis with trypsin (1:50 w/w ratio) and the C-terminal 35 residues were removed by proteolysis with chymotrypsin (1:15 w/w ratio). Following these proteolysis steps, the KcsA channel was further purified by size exclusion chromatography on a Superdex S-200 column using 50 mM Tris- HCl pH 7.5, 150 mM KCl and 0.25 % DM as the column buffer.

Recombinant expression of the control KcsA sample.

The control KcsA sample (without the $^{13}C^{18}O$ isotope labels) was obtained by *in vitro* folding of a recombinantly expressed KcsA polypeptide. For high level expression, the KcsA polypeptide was expressed as a fusion with the ketosteroid isomerase (KSI) fragment [from the pET31b+ vector (EMD Millipore)] that directs expression of the fusion protein to inclusion bodies (*41*). The KcsA polypeptide was designed to carry the same purification tags and amino acid substitutions (S69A, V70C and Y82C) that were present in the semisynthetic KcsA channel. The KSI-KcsA fusion protein was expressed in Rosetta2 (DE3) cells by induction with 1 mM IPTG at an OD_{600} of 1.0 for 3 hours at 37°C. The inclusion bodies (containing the fusion protein) were isolated as previously described (*42*). The inclusion bodies were resuspended in 50 mM Tris-HCl (pH 7.5), 150 mM NaCl, and 1% *N*-laurylsarcosine (NLS) and digested with thrombin (Roche, 1unit/L of culture) overnight, to release the KcsA polypeptide from the KSI fragment. The KcsA polypeptide was purified from the thrombin cleavage mixture using metal affinity chromatography and folded *in vitro* using lipid vesicles. The folded control KcsA channel was purified using metal affinity chromatography followed by size exclusion chromatography as carried out for the semisynthetic channel.

Sample Preparation

One to two microliters of 1.5 mg/mL KcsA in 0.25% (w/v) DM micelles in 50 mM Tris, 150 mM KCl, and 1 mM DTT buffer (pH 7.5) was dried onto a CaF_2 window under a gentle stream of nitrogen. The dried sample was then rehydrated with 5 µL of 99.9% atom% D deuterium oxide (Sigma-Aldrich) and allowed to dry again under nitrogen. This exchange process was repeated ten times until H_2O is replaced by D_2O as measured by the decrease water background and absorption in the frequency range of interest. The sample was then dried down for the final time and rehydrated with 0.1 to 0.2 µL of deuterium oxide for a final sample concentration of 15 mg/mL (3.4 mM) KcsA. The samples were then placed between two CaF_2 windows separated by a 12 µm spacer. Labeled and unlabeled KcsA samples were handled identically.

Two-Dimensional Infrared Measurements

2D IR spectra were collected and processed by methods previously detailed (*36*). Briefly, 800 nm ultrafast pulses were generated by a home-built Ti:Sapphire oscillator pumped by a 532 nm continuous wave laser, which were then amplified in a Nd:YLF-pumped Ti:Sapphire regenerative amplifier. The 800 nm output from the regenerative amplifier was used to pump a home-built β-barium borate (BBO) optical parametric amplifier (OPA) and $AgGaS_2$ difference frequency generation (DFG) setup to produce mid-IR light centered around 6 μm. The ~60 fs mid-IR pulses are then split into pump and probe beams. The pump pulse was sent to a Ge acousto-optic modulator (AOM) pulse shaper to generate our pump pulse pair (*43, 44*), which is spatially and temporally overlapped with the probe pulse at the sample. After the sample, the probe beam was directed into a monochromator and the signal was detected by a mercury cadmium telluride (MCT) array. The resolution along the probe axis is 6 cm^{-1} and along the pump axis it is 3 $cm^{-1.}$ The calibration of our pump and probe frequency axes has been previously described (*36*). Briefly, the calibration of the probe frequencies for each pixel on the MCT detector array was determined by measuring the spectra of ambient water vapor, which is fit the known water vapor spectrum. To calibrate the pump frequency axis, we collect a 2D IR spectrum of the interfering pulse pair on the array detector. The error in calibration is +/- 3 cm^{-1}. One spectrum in our dataset was calibrated according to the procedure described above to which all other spectra were subsequently matched. Spectra are normalized to the unlabeled amide I band. All spectra were taken with a ZZXX polarization scheme.

Molecular Dynamics Simulations

We performed MD simulations using a polarizable force field based on the framework of the classical Drude oscillator for the canonical states as well as the hard-knock states. The force field for the KcsA protein and DPPC lipid molecules are based on the Drude polarizable models, in which the Drude force field explicitly includes atomic polarizability by taking into account the flexible point charge particles associated with heavy atoms (*45, 46*). K^+ and Cl^- parameters that represent improved ion-protein interactions were employed, as reported in a recent study (*31*). The system was solvated with SWM4 water molecules, at an ion concentration of 500 mM (*47*). The starting configurations were taken from equilibrated structures of KcsA, following prior simulations by Roux and coworkers (*48*). To do so, each simulation system was first equilibrated at constant pressure of 1 atm at 298.15 K (*NPT*) followed by production simulation at constant system volume at the same temperature (*NVT*). System temperatures were maintained by coupling to a Langevin thermostat, with temperatures of the Drude particles maintained at 1 K. Electrostatic interactions were summed using the Particle Mesh Ewald (PME) method. Smoothing functions have been applied to both the electrostatics and the van der Waals forces, with real space cutoff of 12 Å and switching function turn on between 10 and 12 Å. A 5 kcal/mol harmonic restraint has been added to the protein CA atoms, excluding those at the selectivity filter region (residues 74 to 79). 100 configurations were generated for each simulation system, at an interval of 20 fs between adjacent frames. Each configuration is then employed as the starting structure for generating the 2D-IR spectroscopy. Systems were first minimized for 3,000 steps at a step size of 0.01 using the steepest decent algorithm, and the GROMOS53a6 force field. 20 ps MD trajectories were then sampled with a 2 fs integration time step. To enforce the configurations of interest, the positions in the filter (residues 74 to 79) were constrained using a spring constant of 2000 $kJ/mol/nm^2$. To avoid generating ambiguous states, coordinates of the K^+

cations in each binding site of the selectivity filter (S0 to S4) were constrained with flat bottom potentials. In both steps of these simulations, water was not constrained. MD packages NAMD2.10 and GROMACS 5.0.4 were employed for simulations using the Drude polarizable force field and the GROMOS53a6 force field, respectively (*49, 50*). This force field is used for the 2D IR simulations because it is the same force field used to develop the correlation of Eq. 1 described below (*51*). It is also important to note that the simulations include configurations in which there is a K^+ ion in the S0 extracellular site. However, the spectra are largely unchanged if the ion in S0 is neglected, because K^+ coordination at S0 does not appreciably alter the frequencies of the isotope labels. Simulations of the knock-on states without water (Fig. S11) in the filter (i.e. [S1, 0, S3, 0] and [0, S2, 0, S4]) were carried out using the same procedure described above.

Calculation of Amide I Spectra

The calculation of amide I 2D IR spectra within the mixed quantum-classical approximation has been described in previous publications (*51-53*). (Note, however, that we avoid the cumulant approximation in this case, unlike Reference (*52*)). The frequencies are calculated based on the projection of the electric fields calculated from the point charges in the classical MD simulation onto the C and N atoms of each amide chromophore, in the C=O bond direction. For the $^{13}C^{18}O$-labeled chromophores examined in this work, the frequency is derived from the electric fields using the relationship (*51*)

$$\omega_{10} = 1618 + 7729E_C - 3576E_N \tag{1}$$

where the frequency ω is in cm^{-1} and the electric fields are in a.u. Note that the zero-field intercept is 66 cm^{-1} lower than the value given in (*51*); this accounts for the frequency shift due to the isotope label (*54*). The second vibrational transition is treated by applying a constant anharmonic shift of Δ = 14 cm^{-1} (so, $\omega_{21} = \omega_{10} - \Delta$).

The frequency shifts due to nearest-neighbor amides are accounted for via a nearest-neighbor frequency shift parameterized based on the relevant Ramachandran angles (*55*). For nearest-neighbor backbone amides, couplings are also calculated from Ramachandran angles (*55*). For other chromophore pairs, the transition dipole coupling scheme of Torii and Tasumi is used (*56*). This scheme also provides the transition dipoles themselves.

With these quantities in hand, the 2D IR spectrum is calculated using a method developed by Liang and Jansen (*53*). In this method, the excitonic wavefunction is initially evenly spread over all amide I local modes; during the delay times, the wavefunction is propagated by dividing the trajectory into a number of short intervals (here, a duration of 20 fs is used) during which the Hamiltonian is assumed to be constant. The fully absorptive 2D IR spectrum is computed by calculating the third-order response functions R_1–R_6 (denoted $S_{GB}^{(I)}$, etc. in (*53*)), multiplying by a factor $\Gamma(t_3, t_2, t_1)$ to account for the vibrational lifetime, performing appropriate Fourier transforms, and summing the imaginary parts of the resulting signals, as in equations 15-18 of (*55*). (Note that the real parts of the signals are summed instead if the proportionality factor $-(i/\hbar)^3$ is ignored, as in (*52*)). The lifetime factor is given by (*53*)

$$\Gamma(t_3, t_2, t_1) = \exp(-(t_3 + 2t_2 + t_1)/2T_1), \tag{2}$$

where t_1 is the time delay between the first and second pulse, t_2 the delay between the second and third pulse, t_3 the delay between the third pulse and the signal, and T_1 the vibrational lifetime (600 fs) (*57*). All theoretical spectra in this work are for the ZZZZ (parallel) polarization combination. For a few of the ion binding configurations, the spectra was also calculated for the ZZXX (perpendicular) polarization combination and found to and were found to only differ from the ZZZZ polarization combination only slightly in the overall intensity of the spectrum. Because the intensity difference is uniform across the different ion configurations, there was no appreciable effect in the linear superposition, and subsequently, the interpretation of the spectra.

Frequencies and couplings were calculated using an in-house code developed as an add-on for GROMACS4.5.1 (*58*). 2D IR spectra were then calculated using the NISE2A code developed by Jansen and co-workers (*53*). Note that the calculations presented in this work include only the labeled amides. Benchmark calculations were performed in which the spectrum was calculated including all amide chromophores in the system, with Val76, Gly77, and Gly79 both labeled and unlabeled. It was found that the difference spectra between the labeled and unlabeled case (which mimics how the experiments were performed) differed very little from the spectra calculated without including the unlabeled amides.

Calculating the nodal line slope

The nodal line slope and the corresponding inverse slope (IS) are a measure of the relative contributions of the spectra from homogeneous and inhomogeneous broadening components (*19, 59*). The nodal line is the region of the 2D spectrum where the positive overtone and negative fundamental peaks overlap, at which the signal intensity is zero. Slices through the peaks at each of the ω_{pump} frequencies along the node were interpolated to determine the corresponding ω_{probe} frequency for the nodal points. The set of ω_{pump} and ω_{probe} for the nodal points was then fit to a line to yield the nodal line slope. The inverse slope (IS) is given by a number between 0 and 1 and was calculated by taking the inverse of the nodal line slope.

Supplementary Text

2D IR Spectra of Labeled and Unlabeled KcsA

Shown in Fig. S3 are 2D IR spectra of labeled and unlabeled KcsA over the complete amide I region of the protein. The most intense pair of peaks absorbs at ω_{pump}=1655 cm^{-1}, which reflects the predominantly alpha-helical structure of KcsA. The absorbance at ω_{pump}=1552 cm^{-1} is the amide II band (not shown) arising from a small fraction of protein that did not deuterium exchange during sample preparation. These spectra closely resemble recently published 2D IR spectra of KcsA by Tokmakoff and coworkers (*20*)The region enclosed in the rectangle is where the absorbances from the $^{13}C^{18}O$ labeled residues appear that are the focus of this report and described in more detail below.

Difference Spectra and Reproducibility

Acid side chains absorb in the frequency range of the $^{13}C^{18}O$ isotope labels, creating a background. To generate a spectrum that highlights the isotope labeled features, we subtracted 2D IR spectra collected for labeled and unlabeled KcsA. For the subtraction, the spectra were normalized to the unlabeled $^{12}C^{16}O$ amide I. To compensate for slight differences in calibration from data set to data set performed on different days, the frequency of the unlabeled KcsA spectrum was adjusted <1 cm^{-1} along each axis to minimize the intensity of the $^{12}C^{16}O$ amide I features in the difference spectrum. This shift is much smaller than the error in frequency calibration and the 2D linewidths and so does not alter the spectral features but does help eliminate the background.

To illustrate and test reproducibility of the data, additional spectra are shown in Fig. S4 and S5 and a statistical analysis is presented in the next section. Each figure contains 2 spectra of unlabeled KcsA and 3 or 4 spectra of isotope labeled KcsA. Difference spectra for each set are shown, created by averaging the labeled and unlabeled spectra, respectively, and subtracting following the procedure above. The difference spectra both exhibit pairs of peaks, which is a strong indicator of reproducibility because the pulse sequence used to generate these 2D IR spectra will produce out-of-phase peaks, as observed. The frequencies of the pairs match to within 5 cm^{-1} and both exhibit elongated lineshapes. The 2D IR spectra shown in the main text of the manuscript (Fig. 2(D) is generated by averaging the difference spectra in Figs. S4 and S5. A statistical analysis is given in the next two sections that quantify the reproducibility of the data.

Statistical Analysis

In this section, we present the statistical analysis of our data to assess the confidence of the difference between labeled and unlabeled spectra. In Table S1, we present the intensity of the pixels corresponding to (ω_{pump}, ω_{probe}) = (1603 cm^{-1}, 1609 cm^{-1}) for N = 7 labeled (I_1) and N = 4 unlabeled (i_1) spectra and (ω_{pump}, ω_{probe}) = (1580 cm^{-1}, 1582 cm^{-1}) for labeled (I_2) and unlabeled (i_2) spectra, respectively. From this data, we tested whether the intensity differences between the labeled and unlabeled peaks are statistically significant by running 2-tailed *t*-tests assuming unequal means and unequal population variances. Table S2 lists the resulting *P* values from the 2-tailed *t*-test. At (ω_{pump}, ω_{probe}) = (1603 cm^{-1}, 1609 cm^{-1}), the difference in intensities between the labeled and unlabeled spectra is statistically significant at the 90% confidence interval. Likewise, we can say with 95% confidence that there is a difference in intensities between the labeled and unlabeled spectra for the pixel corresponding to (ω_{pump}, ω_{probe}) = (1580 cm^{-1}, 1582 cm^{-1}). Therefore, we conclude that the labeled and unlabeled spectra are statistically different from one another with at least 90% confidence.

Experimental Ratio of Intensities

In addition to the above statistical analysis, we look at the ratios of the intensities of the two peaks in the difference spectra. The difference spectra shown in Fig. 2D and Fig. 4A can be calculated in one of two equivalent methods: as a difference of means or as a mean of differences, *Eq. (3)*.

$$\overline{d_p} = \overline{I_p} - \overline{i_p} = \frac{1}{n_I}\sum_{j=1}^{n_I} I_{p,j} - \frac{1}{n_i}\sum_{k=1}^{n_i} i_{p,k} = \frac{1}{n_I n_i}\sum_{j=1}^{n_I}\sum_{k=1}^{n_i}(I_{p,j} - i_{p,k}) \tag{3}$$

where $\overline{d_p}$ is the difference in intensity of the labeled (I) and unlabeled (i) spectra for a particular pixel p for n_I labeled samples and n_i unlabeled samples. In Fig. 2E, we show the integrated volumes (voxels) of the lower frequency peak (peak 2) to the voxel of the higher frequency peak (peak 1) for every one the 28 unique difference spectra created by subtracting combinations of labeled and unlabeled spectra. The voxels were constructed by integrating the intensities of a 3x3 pixel array centered at (ω_{pump}, ω_{probe}) = (1603 cm^{-1}, 1609 cm^{-1}) for peak 1 and (ω_{pump}, ω_{probe}) = (1580 cm^{-1}, 1582 cm^{-1}) for peak 2, respectively. A linear fit of the data provided the ratio of the intensities of the peaks for the difference spectra of 1.25 ± 0.02 with an R-square value of 0.95.

Partial charge of K$^+$ in the selectivity filter

Ab initio calculations find that the charge on K+ depends on its location in the selectivity filter (*35*). To simulate the 2D IR spectra shown in Fig. 3, we used the *ab initio* charges for K$^+$ for each of the four binding sites, which are 100%, 83%, 91%, and 85% for the average z-positions of the oxygens at the S1,S2,S3 and S4 sites, respectively (*35*). The charges were interpolated between these values for z-positions between the binding sites. Since the partial charges for K$^+$ only come from *ab initio* calculations, we tested the effects of K$^+$ partial charge by also simulating 2D IR spectra with a fixed charge of 1.0 for all binding sites, shown in Fig. S6. There is a systematic shift of the isotope labeled peaks by about -20 cm^{-1}, but neither the peak separations nor the linewidths change; the knock-on model still has two pairs of peaks and are elongated whereas the hard-knock model has 1 pair of round peaks. Thus, the precise partial charge the K$^+$ ions does not alter our scientific conclusions.

Simulations of individual isotope labels

We have explored how each of the 3 isotope labels contributes to the 2D IR spectra by simulating the 2D IR spectra for each isotope label individually for each of the 4 ion configurations considered in this manuscript. 2D IR spectra for each of the isotope labels for the two knock-on ion configurations are shown in Fig. S8 (the flipped state spectra are shown in Fig. S9 for these ion binding configurations) and spectra for the hard-knock in Fig. S10. In all cases, the Gly79 isotope labeled carbonyl is broad, weak, and invariant on ion configuration, which is because it is in the S0 site that is on the extracellular side of the filter. Thus, the 2D IR spectra can be interpreted using only the Val76 and Gly77 labels. These two labels are much more elongated (inhomogeneously broadened) in the knock-on than the hard-knock ion configurations, because the filter is more structurally varied (dynamic) in the knock-on model. Gly77 is higher frequency in the [S1,W,S3,W] ion configuration, which makes it sensitive to the knock-on model for ion conduction.

Analysis of the nodal line slope and inverse slope of the 2D spectra

Table 1 summarizes the nodal line slope and inverse slope values obtained for the 2D spectra of the experimental and simulated spectra. The nodal line slope and the inverse slope can be used as a measure of the inhomogeneity of vibrational modes (*19, 59*). A more homogeneous lineshape, indicative of a narrower distribution of structures, is characterized by a steeper nodal line slope (and, consequently, an inverse slope close to 0). Conversely, a more inhomogeneous or elongated lineshape, which reveals a broader distribution of structures, can be characterized by a shallow nodal line slope and an inverse line slope closer to 1. The inhomogeneity of the lineshapes is reflected in the inverse slope, which is three times the value of the inverse slope of the hard-knock configurations. In Fig. 4 and Table 1, we observe that the experimental inverse slope matches the slope obtained from the simulated spectrum of the knock-on configurations with interleaving water molecules, with inverse slope values of about 0.6. Likewise, the inverse slopes of the simulated knock-on without water in the filter and hard-knock ion configurations are significantly smaller than the values obtained for both the experimental and knock-on spectra. Thus, our analysis shows that water is present in the filter of KcsA.

Analysis of the structural distribution in the selectivity filter of the knock-on, knock-on without water hard-knock ion configurations.

To understand the origin of the elongated peaks in the 2D IR spectra of the knock-on ion configurations, we computed the angular distributions of the Val76 and Gly77 carbonyls for each of the 4 ion configurations, shown in Fig. S11. Additionally, we looked at the effects of water on these distributions by removing water from the selectivity filter and rerunning the MD simulation on the knock-on ion configurations without water. We find that both Val76 and Gly77 carbonyls sample up to 36% larger angular variation in the knock-on versus both the knock-on without water and the hard-knock models. The larger angular distributions indicate that the carbonyls in the selectivity filter for the knock-on model is much more flexible and dynamic than the hard-knock model, albeit on timescales that are much longer than the intrinsic time resolution of the 2D IR experiments.

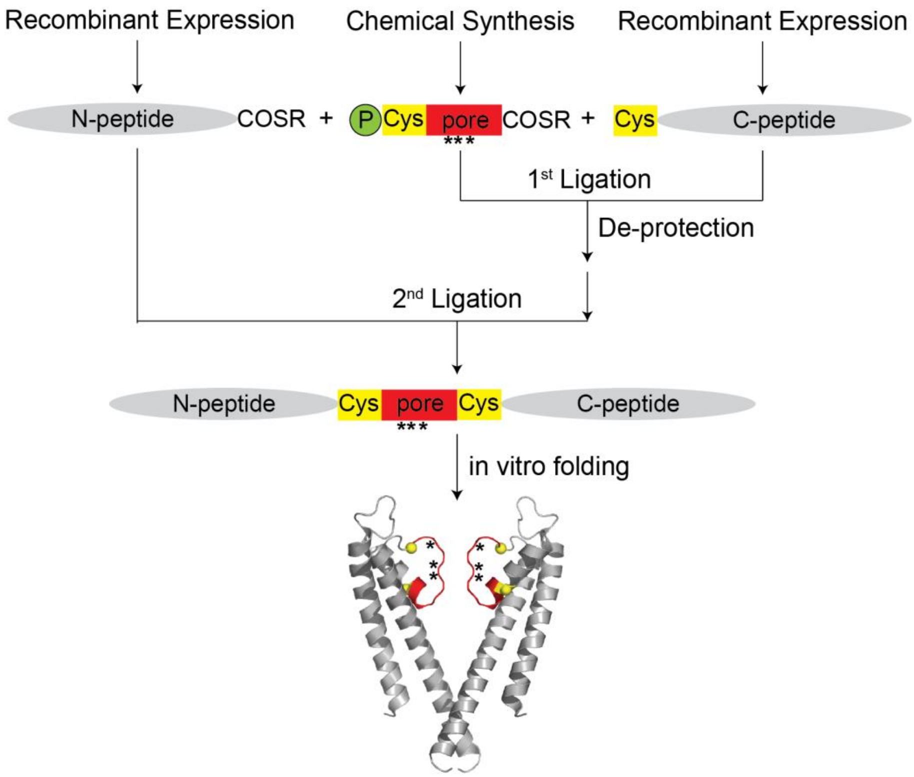

Fig. S1. Strategy for the semisynthesis of the labeled KcsA channel. The KcsA polypeptide is synthesized by two sequential ligation reactions. The first ligation reaction between a recombinantly expressed C-peptide (residues 82- 160) and a chemically synthesized pore peptide (70 -81) yields the intermediate peptide. The $^{13}C^{18}O$ isotopically labeled amino acids in the pore peptide are indicated by an asterisk. The Thz protecting group (green sphere) on the N-terminal cysteine of the intermediate peptide is deprotected, and the intermediate peptide is then ligated to a recombinantly expressed N-peptide thioester (residues 1-69) to yield the KcsA polypeptide. The KcsA polypeptide is folded *in vitro* to the native state. The ligation sites are represented by yellow boxes or spheres.

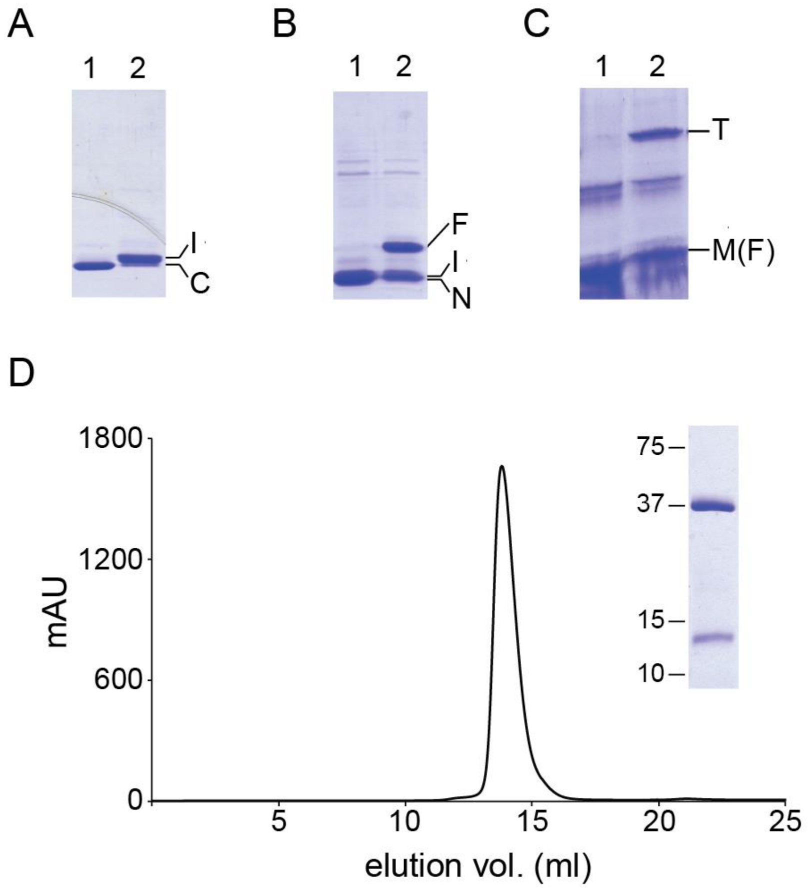

Fig. S2. Semisynthesis of the labeled KcsA. **A**) SDS-PAGE of the first ligation reaction between the C-peptide (C, residues 82-160) and the pore peptide (residues 70_81) to form the intermediate peptide (I, residues 70-160) at 0 min (lane 1) and 2 h (lane 2). **B**) SDS-PAGE of the second ligation reaction between the N-peptide thioester (N, residues 1-69) and the intermediate peptide to form the KcsA polypeptide (F, residues 1-160) at 0 min (lane 1) and 24 h (lane 2). **C**) SDS-PAGE showing the folding of semisynthetic KcsA by lipids. The unfolded monomeric (M, which corresponds to the KcsA polypeptide) and the folded tetrameric KcsA (T) are indicated. **D**) Size exclusion chromatography of the labeled KcsA on a Superdex S200 column indicates an elution volume of 13.8 ml. The control KcsA channel also gave an elution volume of 13.8 ml. Inset: SDS-PAGE gel showing the purified labeled KcsA.

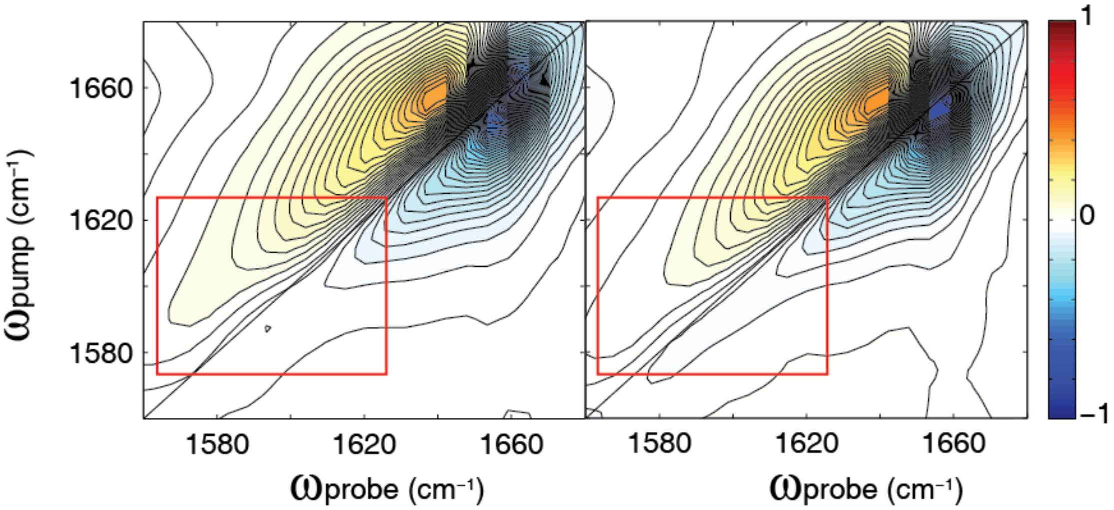

Fig. S3. 2D IR spectra of KcsA. Spectrum of (A) unlabeled and (B) $^{13}C^{18}O$ Val76, Gly77, and Gly79 isotope-labeled KcsA. The red rectangle encloses the region where the $^{13}C^{18}O$ labeled residues are expected to absorb.

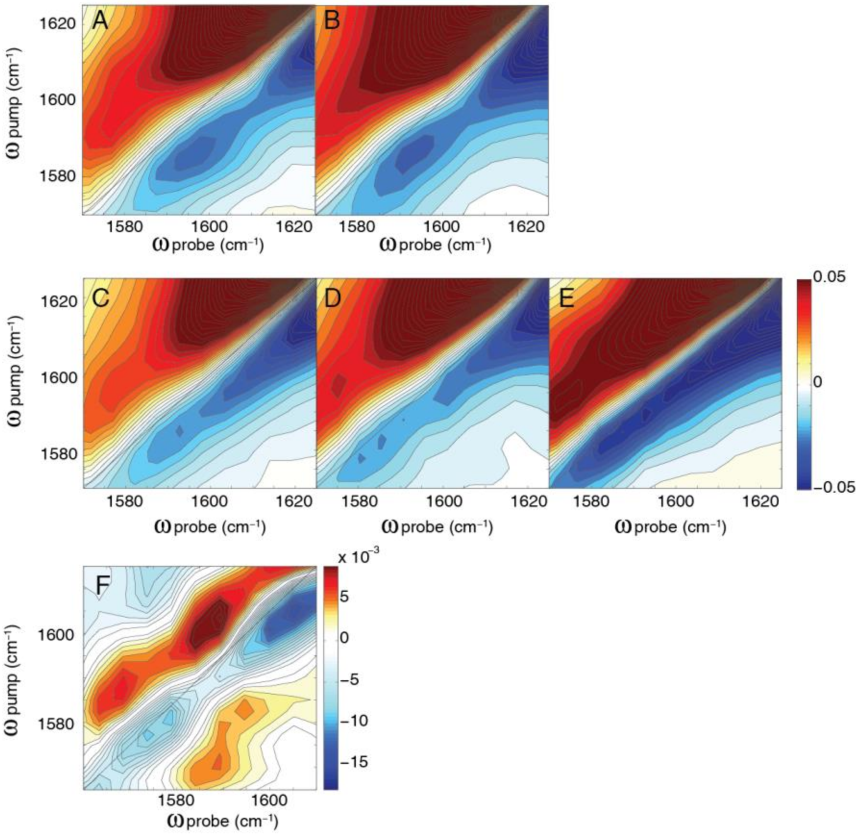

Fig. S4. Additional 2D IR spectra demonstrating reproducibility. (A,B) 2D IR spectra of unlabeled KcsA. (C-E) 2D IR spectra isotope labeled KcsA. (F) Difference spectrum generated from these 5 spectra.

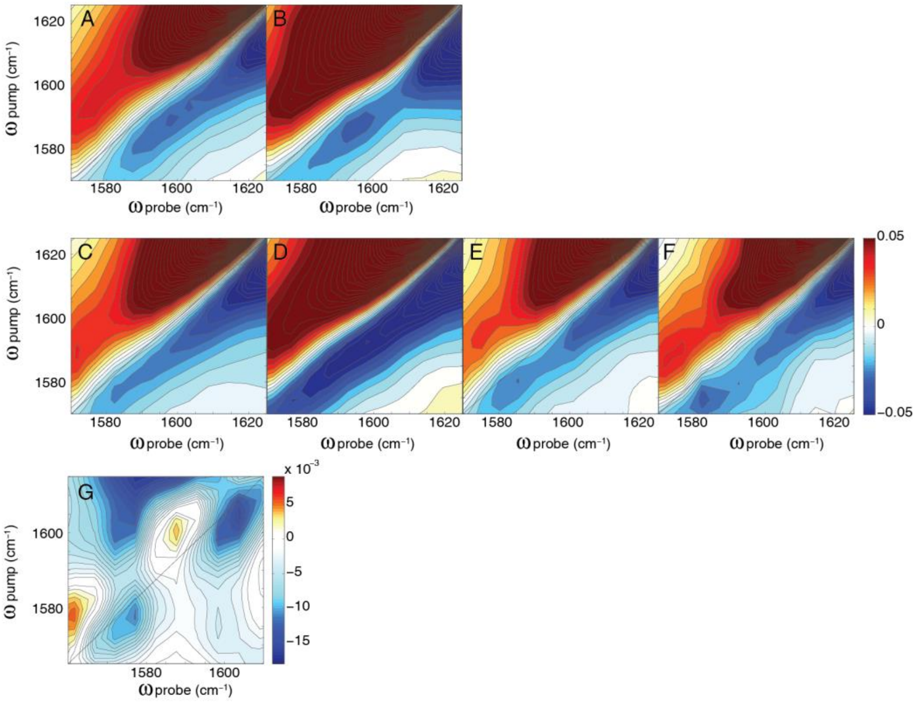

Fig. S5. 2D IR spectra demonstrating reproducibility. (A,B) 2D IR spectra of unlabeled KcsA. (C-F) 2D IR spectra isotope labeled KcsA. (G) Difference spectrum generated from these 6 spectra, which is very similar to that shown in Fig. S5 generated from an entirely different set of spectra.

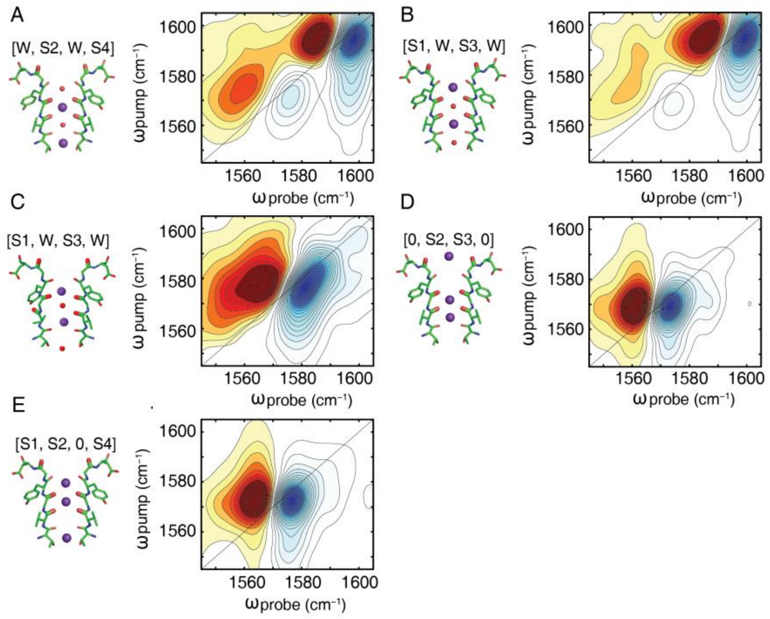

Fig. S6. Calculated 2D IR spectra with 100% K$^+$ charge. The calculated 2D IR spectra of the isotope labels for the (A) [W,S2,W,S4] , (B) [S1,W,S3,W], (C) [S1,W,S3,W] with a Val76 flipped residue, (D) [0,S2,S3,0], and (E) [S1,S2,0,S4] K$^+$ binding conformations. For each of these calculations, the K$^+$ ions in the channel are at 100% K$^+$ charge (i.e. +1 *e*). The spectra are very similar to those presented in the main text of the manuscript (Fig. 3 which used charges based on *ab inito* calculations) except that they absorb about 5-20 cm^{-1} lower in frequency. Regardless of the K+ charge, the spectra are qualitatively similar. Thus, the partial charge of K$^+$ does not alter our scientific conclusions.

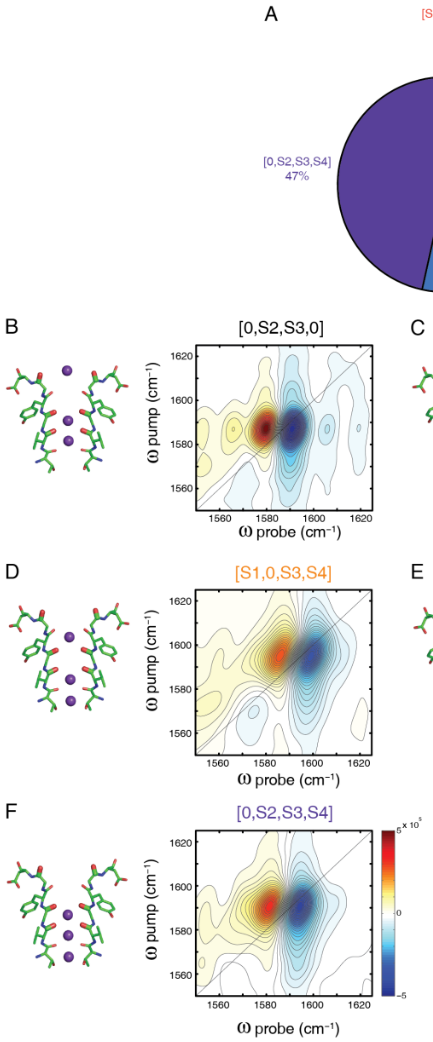

Fig. S7. Calculated 2D IR spectra for the different ion binding configurations of the hard-knock state for the triple. (A) The breakdown of the states constituting the hard-knock mechanism of ion conduction. Adapted from (*17*). (B) Calculated 2D IR spectrum of [0,S2,S3,0] shows a single homogeneous peak at (ω_{pump}, ω_{probe}) = (1587 cm^{-1}, 1591 cm^{-1}). For the (C) [S1,S2,0,S4] state, we see a single peak at (ω_{pump}, ω_{probe}) = (1585 cm^{-1}, 1589 cm^{-1}) . (D) The calculated spectrum for the [S1,0,S3,S4] ion binding configuration reveals two peaks, with the more intense peak at (ω_{pump}, ω_{probe}) = (1595 cm^{-1}, 1599 cm^{-1}) and the less intense peak at (ω_{pump}, ω_{probe}) = (1570 cm^{-1}, 1575 cm^{-1}). In (E), we see a single peak at (ω_{pump}, ω_{probe}) = (1567 cm^{-1}, 1572 cm^{-1}) for the calculated spectrum of [S1,S2,S3,S4]. (F) For the calculated spectrum of the

[0,S2,S3,S4] ion binding configuration, we see a single peak at (ω_{pump}, ω_{probe}) = (1591 cm^{-1}, 1594 cm^{-1}). The weighted sum of the states, using the percentages of each state described in (A), gives us the spectrum shown in Fig. 4D.

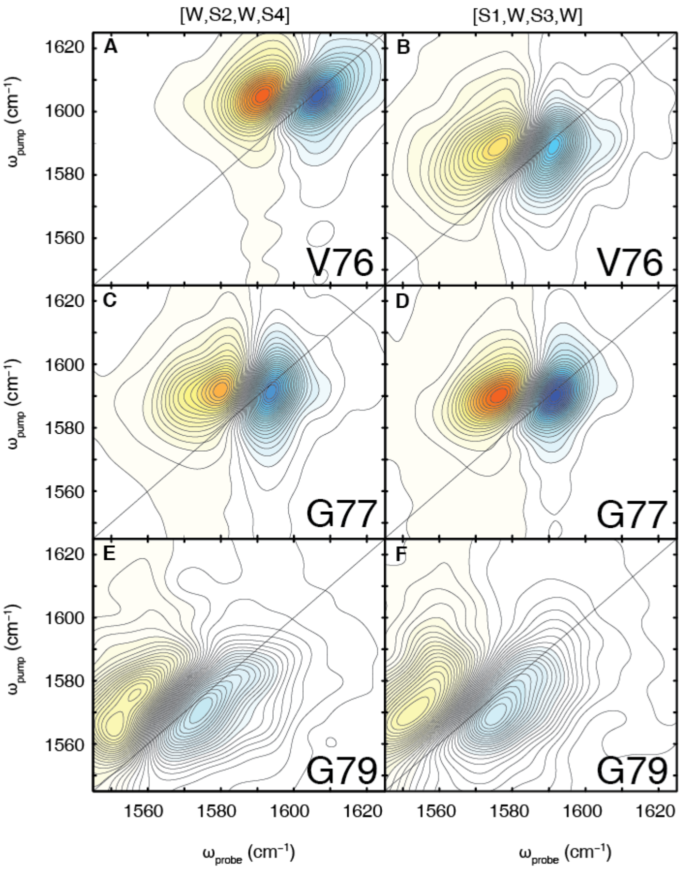

Fig. S8. Calculated spectra for each of the 3 isotope labels in the knock-on conformations in which all Val76 residues point directly into the filter. Shown is the calculated 2D IR spectra for the [W,S2,W,S4] K^+ ion binding configuration for the (A) Val76, (C) Gly77, and (E) Gly79 isotope labels. Val76 absorbs near ω_{pump} = 1605 cm^{-1} and Gly77 at 1591 cm^{-1}. Calculated spectra for the [S1,W,S3,W] K^+ binding configurations for the (B) Val76, (D) Gly77, and (F) Gly79 labels. The Val76 absorbs near 1589 cm^{-1}, and the Gly77 absorbs near 1590 cm^{-1}. The Gly77 frequency does not change between the different ion binding configurations. The Val76 frequency, however, is blueshifted by 16 cm^{-1} when a potassium ion is present in the S2 binding site instead of a water molecule. Also notice that the peaks of the carbonyl directly below the binding site occupied by an ion (i.e. Val76 in the [W,S2,W,S4] configuration and the Gly77 in the [S1,W,S3,W] configuration) are more intense than those coordinating water molecules.

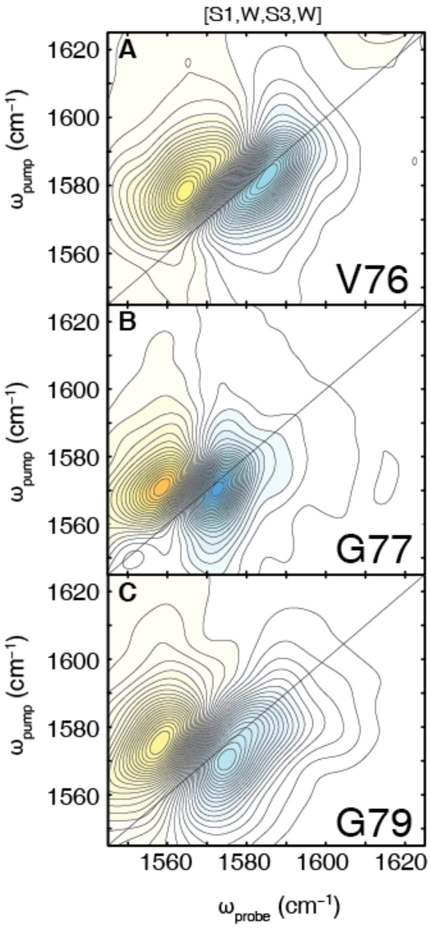

Fig. S9. Calculated spectra for each of the 3 isotope labels in the knock-on conformations in which one of the Val76 residues is pointing out of the filter. Shown is the calculated 2D IR spectra for the Val76 flipped state of the [S1,W,S3,W] K^+ ion binding configuration for the (A) Val76, (B) Gly77, and (C) Gly79 isotope labels. The Val76 absorbs near 1583 cm^{-1}, and the Gly77 absorbs near 1570 cm^{-1}. The flipping of a single Val76 residue outside the filter causes the frequencies of the labels to collectively redshift and broaden in lineshape.

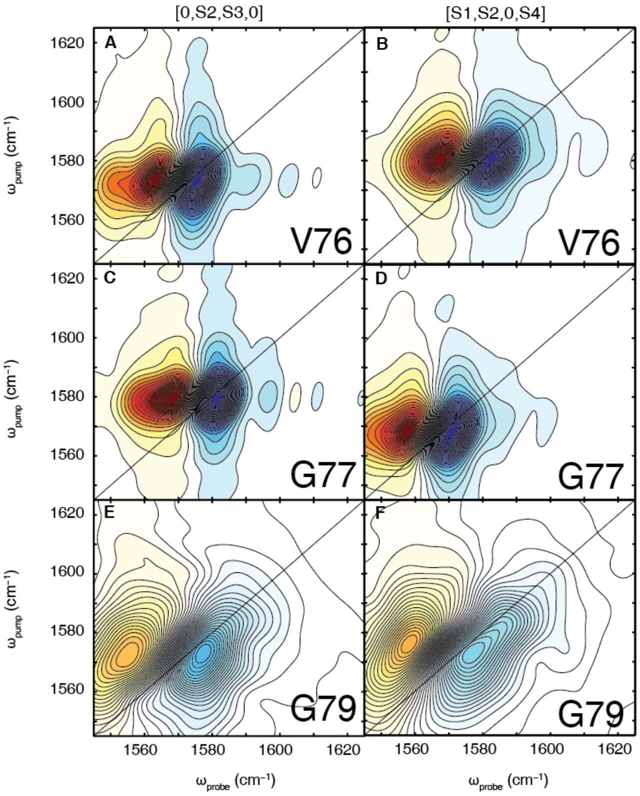

Fig. S10. Calculated spectra for each of the 3 isotope labels in the hard-knock conformations. Shown is the calculated 2D IR spectrum for the [0,S2,S3,0] hard-knock conformation for the (A) Val76, (C) Gly77, and (E) Gly79 isotope labels. Val76 and Gly77, which are the most intense, are homogeneous. All labels absorb near ω_{pump} = 1580 cm^{-1}. The calculated spectra for the [S1,S2,0,S4] K^{+} binding configurations are also shown for the (B) Val76, (D), Gly77, and (F) Gly79 isotope labels. Again, the Val76 and Gly77 labels are the most intense and have very homogeneous lineshapes.

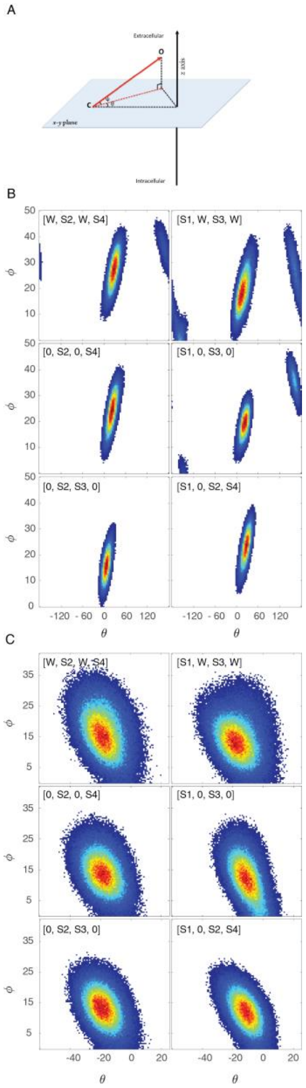

Fig. S11. Distribution of carbonyl angles (θ, φ) at the ion binding sites in the selectivity filter for the knock-on and hard-knock configurations from MD simulations. (A) For this analysis, φ is defined as the z-axis component of the carbonyl dipole, where the z-axis is the axis of ion conduction. The θ angle is defined as the projection of the carbonyl dipole. (B) Distribution of (θ, φ) angles for Val76 carbonyl dipoles. The states for the filter are shown in the top left corner. We can see that for the knock-on conformations (first row), the θ and φ angles have a wider distribution than those of the knock-on conformations without water (second row) or those of the hard-knock conformations (third row). (C) The distribution of (θ, φ) angles for the Gly77 carbonyl. The carbonyls for the knock-on ion configuration (first row) sample a broader range of θ and φ angles than the knock-on configuration without water (second row) or the hard-knock states (third row). The analysis of the MD simulations indicates that the carbonyl groups in the knock-on state are more dynamic than those observed in the knock-on state without water and the hard-knock state.

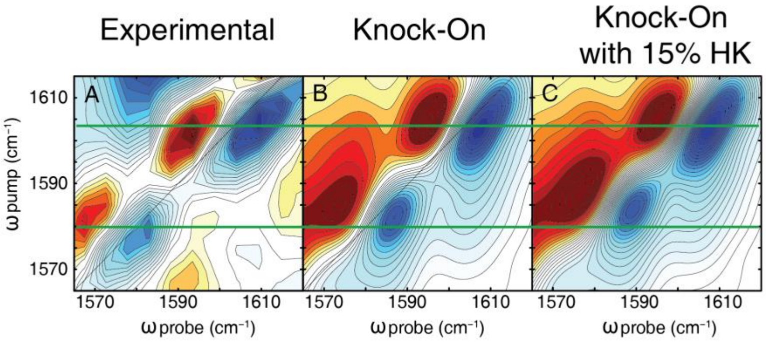

Fig. S12. Incorporation of both knock-on and hard-knock models reveals that knock-on ion binding configurations are dominant configurations. (A) Experimental spectrum from Fig. 2D. (B) Spectrum from Fig. 4B of calculated 2D IR spectrum of a linear combination of [W,S2,W,S4], [S1,W,S3,W] and [S1,W,S3,W] with a single Val76 residue flipped out of the filter. The ratios used to reproduce the experimental spectrum are 0.3:0.3:0.4, respectively. (C) Linear combination of hard-knock states from Fig. 4C along with the ion binding configurations [W,S2,W,S4], [S1,W,S3,W] and [S1,W,S3,W] with a single Val76 residue flipped out of the filter reveal that the hard-knock state cannot account for more than 15% of the ion binding configurations. Increasing the percentage of hard-knock states beyond 15% decreases the frequency separation of the two peaks and affects the observed lineshape.

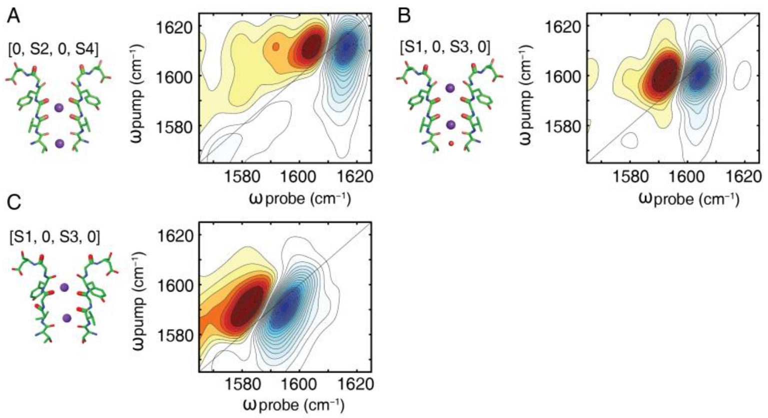

Fig. S13. Calculated 2D IR spectra of knock-on states without water. To see the changes to the calculated spectra in the absence of water in the filter, simulations of the two knock-on states ([W,S2,W,S4] and [S1,W,S3,W]) were run without water in the filter (i.e. [0,S2,0,S4] and [S1,0,S3,0], respectively). (A) The calculated 2D IR spectrum for the [0,S2,0,S4] state reveals that the frequency of the vibrational modes change by approximately 4 cm^{-1}, and the shape of the peak becomes slightly more homogeneous if we exclude water from the filter. For (B), the [S1,0,S3,0] state, we see no change in the spectrum with the removal of water. (C) The absence of water in the Val76 flipped [S1,0,S3,0] does not affect the lineshapes nor the frequencies relative to the hydrated state. Adding the [0,S2,0,S4] and [S1,0,S3,0] (unflipped and flipped) spectra together in the ratios 0.3:0.3:0.4 , respectively, yields Fig. 4D. Analysis of these ion binding configurations without water shows that any combination of these spectra will not generate a spectrum that matches the experiment. Therefore, we conclude from this analysis that water is present in the filter.

Table S1: Intensities (AU) of pixels corresponding to (ω_{pump}, ω_{probe}) = (1603 cm^{-1}, 1609 cm^{-1}) for labeled (I_1) and unlabeled (i_1) spectra and (ω_{pump}, ω_{probe}) = (1580 cm^{-1}, 1582 cm^{-1}) for labeled (I_2) and unlabeled (i_2) spectra, respectively.

Sample	**Labeled Intensity I_1 (AU)**	**Labeled Intensity I_2 (AU)**	**Unlabeled Intensity i_1 (AU)**	**Unlabeled Intensity i_2 (AU)**
1	-0.0343	-0.0196	-0.0222	-0.0143
2	-0.0269	-0.0142	-0.0130	-0.0086
3	-0.0295	-0.0218	-0.0324	-0.0155
4	-0.0609	-0.0455	-0.0233	-0.0182
5	-0.0409	-0.0245		
6	-0.0604	-0.0449		
7	-0.0194	-0.0212		

Table S2: *P* values from 2-tailed *t*-test

	Unlabeled Intensity i_1 (AU)	**Unlabeled Intensity i_2 (AU)**
Labeled Intensity I_1 (AU)	0.0579	
Labeled Intensity I_2 (AU)		0.0373

Table S3. Fitted values for the nodal line slope and inverse slope for experimental and simulated 2D IR spectra. The nodal line slope was calculated as described for the experimental high and low frequency peaks, knock-on high and low frequency peaks, and hard-knock peak, respectively. The inverse slope was calculated by taking the inverse of the nodal line slope.

Spectrum	**Center ω_{pump} (cm^{-1})**	**Nodal Line Slope**	**Inverse Slope**
Experimental	1603	1.72 ± 0.01	0.58 ± 0.01
	1580	1.68 ± 0.18	0.60 ± 0.11
Knock-On	1603	1.98 ± 0.06	0.51 ± 0.03
	1582	1.91 ± 0.17	0.52 ± 0.09
Hard-Knock	1587	3.73 ± 0.09	0.26 ± 0.03
Knock-On Without Water	1599	2.75 ± 0.46	0.36 ± 0.17

References

1. B. Hille, *Ion Channels of Excitable Membranes* (Sinauer Associates, Inc., Sunderland, MA, 2001).

2. L. Heginbotham, T. Abramson, R. MacKinnon, A functional connection between the pores of distantly related ion channels as revealed by mutant K^+ channels. *Science* **258**, 1152–1155 (1992). Medline doi:10.1126/science.1279807

3. D. A. Doyle, J. Morais Cabral, R. A. Pfuetzner, A. Kuo, J. M. Gulbis, S. L. Cohen, B. T. Chait, R. MacKinnon, The structure of the potassium channel: Molecular basis of K^+ conduction and selectivity. *Science* **280**, 69–77 (1998). Medline doi:10.1126/science.280.5360.69

4. A. L. Hodgkin, R. D. Keynes, The potassium permeability of a giant nerve fibre. *J. Physiol.* **128**, 61–88 (1955). Medline doi:10.1113/jphysiol.1955.sp005291

5. S. Uysal, V. Vásquez, V. Tereshko, K. Esaki, F. A. Fellouse, S. S. Sidhu, S. Koide, E. Perozo, A. Kossiakoff, Crystal structure of full-length KcsA in its closed conformation. *Proc. Natl. Acad. Sci. U.S.A.* **106**, 6644–6649 (2009). Medline doi:10.1073/pnas.0810663106

6. J. H. Morais-Cabral, Y. Zhou, R. MacKinnon, Energetic optimization of ion conduction rate by the K^+ selectivity filter. *Nature* **414**, 37–42 (2001). Medline doi:10.1038/35102000

7. A. N. Thompson, I. Kim, T. D. Panosian, T. M. Iverson, T. W. Allen, C. M. Nimigean, Mechanism of potassium-channel selectivity revealed by Na^+ and Li^+ binding sites within the KcsA pore. *Nat. Struct. Mol. Biol.* **16**, 1317–1324 (2009). Medline doi:10.1038/nsmb.1703

8. S. Y. Noskov, S. Bernèche, B. Roux, Control of ion selectivity in potassium channels by electrostatic and dynamic properties of carbonyl ligands. *Nature* **431**, 830–834 (2004). Medline doi:10.1038/nature02943

9. Y. Zhou, R. MacKinnon, The occupancy of ions in the K^+ selectivity filter: Charge balance and coupling of ion binding to a protein conformational change underlie high conduction rates. *J. Mol. Biol.* **333**, 965–975 (2003). Medline doi:10.1016/j.jmb.2003.09.022

10. S. Bernèche, B. Roux, Energetics of ion conduction through the K^+ channel. *Nature* **414**, 73–77 (2001). Medline doi:10.1038/35102067

11. S. Bernèche, B. Roux, A microscopic view of ion conduction through the K^+ channel. *Proc. Natl. Acad. Sci. U.S.A.* **100**, 8644–8648 (2003). Medline doi:10.1073/pnas.1431750100

12. C. Alcayaga, X. Cecchi, O. Alvarez, R. Latorre, Streaming potential measurements in $Ca2^+$-activated K^+ channels from skeletal and smooth muscle. Coupling of ion and water fluxes. *Biophys. J.* **55**, 367–371 (1989). Medline doi:10.1016/S0006-3495(89)82814-0

13. M. Iwamoto, S. Oiki, Counting ion and water molecules in a streaming file through the open-filter structure of the K channel. *J. Neurosci.* **31**, 12180–12188 (2011). Medline doi:10.1523/JNEUROSCI.1377-11.2011

14. J. Åqvist, V. Luzhkov, Ion permeation mechanism of the potassium channel. *Nature* **404**, 881–884 (2000). Medline doi:10.1038/35009114

15. S. Furini, C. Domene, Atypical mechanism of conduction in potassium channels. *Proc. Natl. Acad. Sci. U.S.A.* **106**, 16074–16077 (2009). Medline doi:10.1073/pnas.0903226106

16. P. W. Fowler, E. Abad, O. Beckstein, M. S. Sansom, Energetics of multi-ion conduction pathways in potassium ion channels. *J. Chem. Theory Comput.* **9**, 5176–5189 (2013). Medline doi:10.1021/ct4005933

17. D. A. Köpfer, C. Song, T. Gruene, G. M. Sheldrick, U. Zachariae, B. L. de Groot, Ion permeation in K^+ channels occurs by direct Coulomb knock-on. *Science* **346**, 352–355 (2014). Medline doi:10.1126/science.1254840

18. S. D. Fried, S. Bagchi, S. G. Boxer, Measuring electrostatic fields in both hydrogen-bonding and non-hydrogen-bonding environments using carbonyl vibrational probes. *J. Am. Chem. Soc.* **135**, 11181–11192 (2013). Medline doi:10.1021/ja403917z

19. A. Ghosh, J. Qiu, W. F. DeGrado, R. M. Hochstrasser, Tidal surge in the M2 proton channel, sensed by 2D IR spectroscopy. *Proc. Natl. Acad. Sci. U.S.A.* **108**, 6115–6120 (2011). Medline doi:10.1073/pnas.1103027108

20. P. Stevenson, C. Götz, C. R. Baiz, J. Akerboom, A. Tokmakoff, A. Vaziri, Visualizing KcsA conformational changes upon ion binding by infrared spectroscopy and atomistic modeling. *J. Phys. Chem. B* **119**, 5824–5831 (2015). Medline doi:10.1021/acs.jpcb.5b02223

21. F. I. Valiyaveetil, R. MacKinnon, T. W. Muir, Semisynthesis and folding of the potassium channel KcsA. *J. Am. Chem. Soc.* **124**, 9113–9120 (2002). Medline doi:10.1021/ja0266722

22. A. G. Komarov, K. M. Linn, J. J. Devereaux, F. I. Valiyaveetil, Modular strategy for the semisynthesis of a K^+ channel: Investigating interactions of the pore helix. *ACS Chem. Biol.* **4**, 1029–1038 (2009). Medline doi:10.1021/cb900210r

23. J. Torres, A. Kukol, J. M. Goodman, I. T. Arkin, Site-specific examination of secondary structure and orientation determination in membrane proteins: The peptidic $^{13}C{=}^{18}O$ group as a novel infrared probe. *Biopolymers* **59**, 396–401 (2001). Medline doi:10.1002/1097-0282(200111)59:6<396::AID-BIP1044>3.0.CO;2-Y

24. Z. Ganim, A. Tokmakoff, A. Vaziri, Vibrational excitons in ionophores: Experimental probes for quantum coherence-assisted ion transport and selectivity in ion channels. *New J. Phys.* **13**, 113030 (2011). doi:10.1088/1367-2630/13/11/113030

25. A. Barth, The infrared absorption of amino acid side chains. *Prog. Biophys. Mol. Biol.* **74**, 141–173 (2000). Medline doi:10.1016/S0079-6107(00)00021-3

26. A. Barth, C. Zscherp, What vibrations tell us about proteins. *Q. Rev. Biophys.* **35**, 369–430 (2002). Medline doi:10.1017/S0033583502003815

27. H. Kim, M. Cho, Infrared probes for studying the structure and dynamics of biomolecules. *Chem. Rev.* **113**, 5817–5847 (2013). Medline doi:10.1021/cr3005185

28. Y. S. Kim, R. M. Hochstrasser, Applications of 2D IR spectroscopy to peptides, proteins, and hydrogen-bond dynamics. *J. Phys. Chem. B* **113**, 8231–8251 (2009). Medline doi:10.1021/jp8113978

29. S. Bernèche, B. Roux, A gate in the selectivity filter of potassium channels. *Structure* **13**, 591–600 (2005). Medline doi:10.1016/j.str.2004.12.019

30. P. Hamm, M. T. Zanni, *Concepts and Methods of 2D Infrared Spectroscopy*. (Cambridge University Press, New York, 2011).

31. H. Li, V. Ngo, M. C. Da Silva, D. R. Salahub, K. Callahan, B. Roux, S. Y. Noskov, Representation of ion-protein interactions using the Drude polarizable force-field. *J. Phys. Chem. B* **119**, 9401–9416 (2015). Medline doi:10.1021/jp510560k

32. C. R. Baiz, Y. S. Lin, C. S. Peng, K. A. Beauchamp, V. A. Voelz, V. S. Pande, A. Tokmakoff, A molecular interpretation of 2D IR protein folding experiments with Markov state models. *Biophys. J.* **106**, 1359–1370 (2014). Medline doi:10.1016/j.bpj.2014.02.008

33. C. R. Schwantes, V. S. Pande, Improvements in Markov state model construction reveal many non-native interactions in the folding of NTL9. *J. Chem. Theory Comput.* **9**, 2000–2009 (2013). Medline doi:10.1021/ct300878a

34. L. Leisle, F. Valiyaveetil, R. A. Mehl, C. A. Ahern, in *Novel Chemical Tools to Study Ion Channel Biology,* C. Ahern, S. Pless, Eds. (Springer, New York, 2015), vol. 869, chap. 7, pp. 119–151.

35. S. Kraszewski, C. Boiteux, C. Ramseyer, C. Girardet, Determination of the charge profile in the KcsA selectivity filter using ab initio calculations and molecular dynamics simulations. *Phys. Chem. Chem. Phys.* **11**, 8606–8613 (2009). Medline doi:10.1039/b905991a

36. C. T. Middleton, A. M. Woys, S. S. Mukherjee, M. T. Zanni, Residue-specific structural kinetics of proteins through the union of isotope labeling, mid-IR pulse shaping, and coherent 2D IR spectroscopy. *Methods* **52**, 12–22 (2010). Medline doi:10.1016/j.ymeth.2010.05.002

37. M. S. Seyfried, B. S. Lauber, N. W. Luedtke, Multiple-turnover isotopic labeling of Fmoc- and Boc-protected amino acids with oxygen isotopes. *Org. Lett.* **12**, 104–106 (2010). Medline doi:10.1021/ol902519g

38. A. G. Komarov, C. A. Costantino, F. I. Valiyaveetil, Engineering K^+ channels using semisynthesis. *Methods Mol. Biol.* **995**, 3–17 (2013). Medline doi:10.1007/978-1-62703-345-9_1

39. A. Sivashanmugam, V. Murray, C. Cui, Y. Zhang, J. Wang, Q. Li, Practical protocols for production of very high yields of recombinant proteins using *Escherichia coli*. *Protein Sci.* **18**, 936–948 (2009). Medline doi:10.1002/pro.102

40. D. Bang, S. B. Kent, A one-pot total synthesis of crambin. *Angew. Chem. Int. Ed. Engl.* **43**, 2534–2538 (2004). Medline doi:10.1002/anie.200353540

41. P. M. Hwang, J. S. Pan, B. D. Sykes, Targeted expression, purification, and cleavage of fusion proteins from inclusion bodies in *Escherichia coli*. *FEBS Lett.* **588**, 247–252 (2014). Medline doi:10.1016/j.febslet.2013.09.028

42. P. K. Devaraneni, J. J. Devereaux, F. I. Valiyaveetil, In vitro folding of KvAP, a voltage-gated K^+ channel. *Biochemistry* **50**, 10442–10450 (2011). Medline doi:10.1021/bi2012965

43. S. H. Shim, D. B. Strasfeld, M. T. Zanni, Generation and characterization of phase and amplitude shaped femtosecond mid-IR pulses. *Opt. Express* **14**, 13120–13130 (2006). Medline doi:10.1364/OE.14.013120

44. S. H. Shim, D. B. Strasfeld, Y. L. Ling, M. T. Zanni, Automated 2D IR spectroscopy using a mid-IR pulse shaper and application of this technology to the human islet amyloid polypeptide. *Proc. Natl. Acad. Sci. U.S.A.* **104**, 14197–14202 (2007). Medline doi:10.1073/pnas.0700804104

45. P. E. M. Lopes, J. Huang, J. Shim, Y. Luo, H. Li, B. Roux, A. D. Mackerell Jr., Polarizable force field for peptides and proteins based on the classical Drude oscillator. *J. Chem. Theory Comput.* **9**, 5430–5449 (2013). Medline doi:10.1021/ct400781b

46. J. Chowdhary, E. Harder, P. E. Lopes, L. Huang, A. D. MacKerell Jr., B. Roux, A polarizable force field of dipalmitoylphosphatidylcholine based on the classical Drude model for molecular dynamics simulations of lipids. *J. Phys. Chem. B* **117**, 9142–9160 (2013). Medline doi:10.1021/jp402860e

47. G. Lamoureux, E. Harder, I. V. Vorobyov, B. Roux, A. D. MacKerell Jr., A polarizable model of water for molecular dynamics simulations of biomolecules. *Chem. Phys. Lett.* **418**, 245–249 (2006). doi:10.1016/j.cplett.2005.10.135

48. C. N. Rowley, B. Roux, A computational study of barium blockades in the KcsA potassium channel based on multi-ion potential of mean force calculations and free energy perturbation. *J. Gen. Physiol.* **142**, 451–463 (2013). Medline doi:10.1085/jgp.201311049

49. J. C. Phillips, R. Braun, W. Wang, J. Gumbart, E. Tajkhorshid, E. Villa, C. Chipot, R. D. Skeel, L. Kalé, K. Schulten, Scalable molecular dynamics with NAMD. *J. Comput. Chem.* **26**, 1781–1802 (2005). Medline doi:10.1002/jcc.20289

50. D. Van Der Spoel, E. Lindahl, B. Hess, G. Groenhof, A. E. Mark, H. J. Berendsen, GROMACS: Fast, flexible, and free. *J. Comput. Chem.* **26**, 1701–1718 (2005). Medline doi:10.1002/jcc.20291

51. L. Wang, C. T. Middleton, M. T. Zanni, J. L. Skinner, Development and validation of transferable amide I vibrational frequency maps for peptides. *J. Phys. Chem. B* **115**, 3713–3724 (2011). Medline doi:10.1021/jp200745r

52. L. Wang, C. T. Middleton, S. Singh, A. S. Reddy, A. M. Woys, D. B. Strasfeld, P. Marek, D. P. Raleigh, J. J. de Pablo, M. T. Zanni, J. L. Skinner, 2DIR spectroscopy of human amylin fibrils reflects stable β-sheet structure. *J. Am. Chem. Soc.* **133**, 16062–16071 (2011). Medline doi:10.1021/ja204035k

53. C. Liang, T. L. C. Jansen, An efficient N^3-scaling propagation scheme for simulating two-dimensional infrared and visible spectra. *J. Chem. Theory Comput.* **8**, 1706–1713 (2012). Medline doi:10.1021/ct300045c

54. A. M. Woys, A. M. Almeida, L. Wang, C. C. Chiu, M. McGovern, J. J. de Pablo, J. L. Skinner, S. H. Gellman, M. T. Zanni, Parallel β-sheet vibrational couplings revealed by 2D IR spectroscopy of an isotopically labeled macrocycle: Quantitative benchmark for the interpretation of amyloid and protein infrared spectra. *J. Am. Chem. Soc.* **134**, 19118–19128 (2012). Medline doi:10.1021/ja3074962

55. T. la Cour Jansen, A. G. Dijkstra, T. M. Watson, J. D. Hirst, J. Knoester, Modeling the amide I bands of small peptides. *J. Chem. Phys.* **125**, 044312 (2006). Medline doi:10.1063/1.2218516

56. H. Torii, M. Tasumi, Ab initio molecular orbital study of the amide I vibrational interactions between the peptide groups in di- and tripeptides and considerations on the conformation of the extended helix. *J. Raman Spectrosc.* **29**, 81–86 (1998). doi:10.1002/(SICI)1097-4555(199801)29:1<81::AID-JRS214>3.0.CO;2-H

57. P. Mukherjee, A. T. Krummel, E. C. Fulmer, I. Kass, I. T. Arkin, M. T. Zanni, Site-specific vibrational dynamics of the CD3ζ membrane peptide using heterodyned two-dimensional infrared photon echo spectroscopy. *J. Chem. Phys.* **120**, 10215–10224 (2004). Medline doi:10.1063/1.1718332

58. B. Hess, C. Kutzner, D. van der Spoel, E. Lindahl, GROMACS 4: Algorithms for highly efficient, load-balanced, and scalable molecular simulation. *J. Chem. Theory Comput.* **4**, 435–447 (2008). Medline doi:10.1021/ct700301q

59. Y. S. Kim, L. Liu, P. H. Axelsen, R. M. Hochstrasser, 2D IR provides evidence for mobile water molecules in beta-amyloid fibrils. *Proc. Natl. Acad. Sci. U.S.A.* **106**, 17751–17756 (2009). Medline doi:10.1073/pnas.0909888106